Evidence of metamaterial physics at the geophysics scale: the METAFORET experiment

Journal Article

Author(s):
Lott, Martin; Roux, Philippe; Garambois, Stéphane; Guéguen, Philippe; Colombi, Andrea

Evidence of metamaterial physics at the geophysics scale: the METAFORET experiment

Martin Lott,[1] Philippe Roux,[1] Stéphane Garambois [ORCID],[1] Philippe Guéguen[1] and Andrea Colombi[2]

[1]*University Grenoble Alpes, University Savoie Mont Blanc, CNRS, IRD, IFSTTAR, ISTerre, 38000 Grenoble, France.*
E-mail: martin.lott@univ-grenoble-alpes.fr
[2]*Department of Civil, Environmental and Geomatic Engineering, Institute of Structural Engineering, Swiss Federal Institute of Technology, Zurich, Switzerland*

SUMMARY

The METAFORET experiment was designed to demonstrate that complex wave physics phenomena classically observed at the meso- and microscales in acoustics and in optics also apply at the geophysics scale. In particular, the experiment shows that a dense forest of trees can behave as a locally resonant metamaterial for seismic surface waves. The dense arrangement of trees anchored into the ground creates anomalous dispersion curves for surface waves, which highlight a large frequency band-gap around one resonant frequency of the trees, at ∼45 Hz. This demonstration is carried out through the deployment of a dense seismic array of ∼1000 autonomous geophones providing seismic recordings under vibrating source excitation at the transition between an open field and a forest. Additional geophysical equipment was deployed (e.g. ground-penetrating radar, velocimeters on trees) to provide essential complementary measurements. Insights and interpretations on the observed seismic wavefield, including the attenuation length, the intensity ratio between the field and the forest and the surface wave polarization, are validated with 2-D numerical simulations of trees over a layered half-space.

Key words: Numerical modelling; Spatial analysis; Acoustic properties; Guided waves; Wave scattering and diffraction.

1 INTRODUCTION

Research conducted across the 1990s on structured materials for both electromagnetic and mechanical waves control has brought to the foreground the concept of locally resonant metamaterials. In these media the coupling between subwavelength resonators yield unique dispersion properties well suited to shape the wave propagation at will (Liu *et al.* 2000; Pendry *et al.* 2006). The fundamental nature and robustness of metamaterial physics were investigated by experiments that ranged from optical wave manipulation to acoustic experimentation (Milton *et al.* 2006; Brun *et al.* 2009). Other laboratory-scale investigations of the propagation of elastic surface waves in thin plates and supported by numerical experiments have been performed to illustrate the application of metamaterial physics to wave control in plates (Farhat *et al.* 2009; Rupin *et al.* 2014). It was then demonstrated for all wave types that the mesoscale behaviour of a composite material that consists of resonant elements with spatial disorder at the subwavelength scale is controlled by the dispersive nature of its coupled resonators (Liu *et al.* 2000; Pendry 2000; Engheta & Ziolkowski 2006; Achaoui *et al.* 2011). Among the properties characterizing metamaterials, their capacity to create bandgaps, that is frequency bands of forbidden wave propagation,

has potential for novel applications in mechanics and civil engineering (e.g. vibration containment, wave channeling and even seismic attenuation).

Metamaterial physics was recently studied at the geophysics scale for seismic waves (Brûlé *et al.* 2014; Roux *et al.* 2018; Krödel *et al.* 2015), hence by upscaling designs originally developed in the laboratory, to investigate the behaviour of so-called seismic metamaterials. An ambitious study carried out in October 2016, the METAFORET experiment (https://metaforet.osug.fr/), consisted of the deployment of a large number of receivers in the Landes Forest (Southwest France), over 2 weeks. The unaliased spatial sampling of the complex forest wavefield across a wide range of frequencies includes the bandgap target range of 40–50 Hz that was suggested in a preliminary numerical study (Colombi *et al.* 2016a). This sampling requires a dense seismic network that consists of >1000 seismic instruments spread over an area of 120 m × 120 m (Fig. 1). All of the relevant aspects of the dense array continuous recording systems were presented recently (Roux *et al.* 2018), including: (1) the seismic vibrator source used to excite high-frequency (>20 Hz) transient wave fields; (2) the ground-penetrating radar (GPR) survey for high-resolution imaging of the top 2 m and (3) the comparison with records of the tree-mounted velocimeters to illustrate
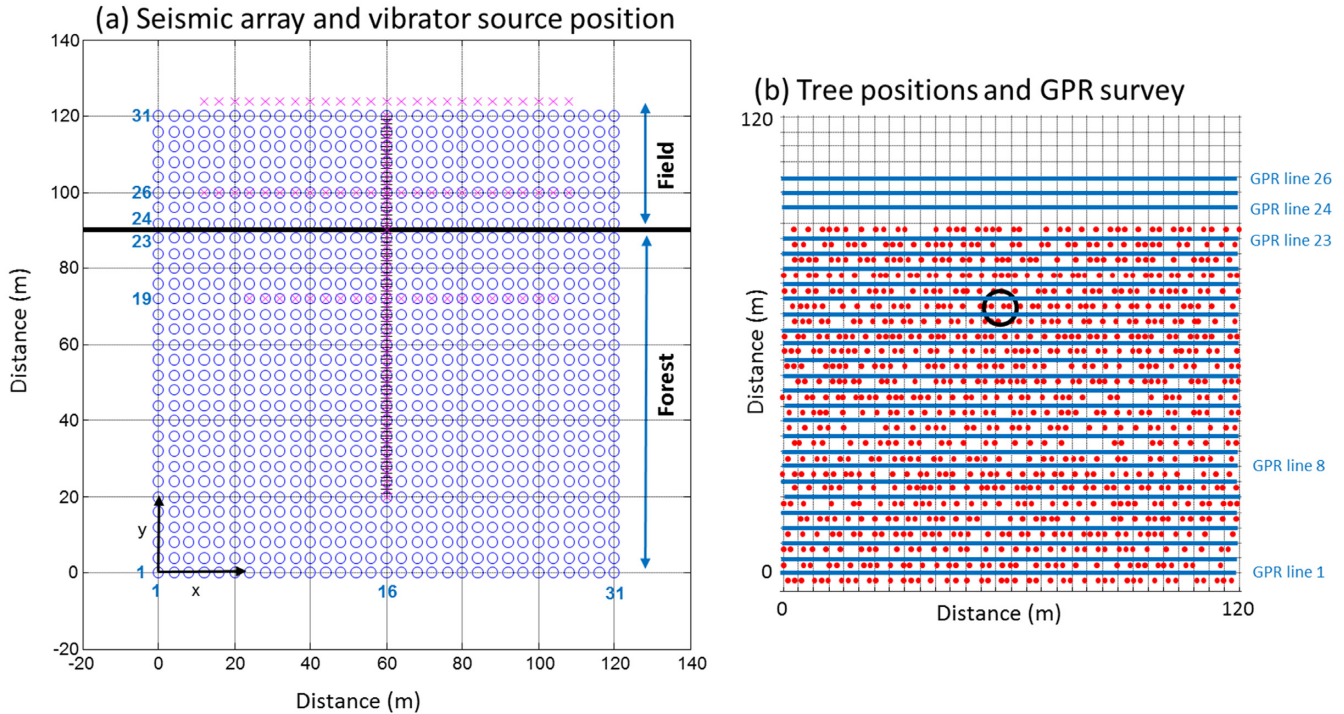
Figure 1. Geometry of the METAFORET experiment. (a) Spatial representation of the 2-D seismic array, which is composed of 31×31 vertical Z-land sensors (blue circles) and three-component GIPP instruments positioned as a 100-sensor line array (black '+' marks) that crosses the boundary between the field and the forest (horizontal bold black line). The shaker source was positioned sequentially at 122 different locations (pink 'x' marks), which involved three lines of sources along the x-axis and one line along the y-axis. Some column and row numbers (blue) have been added on the left and bottom sides of the two dimensions. (b) Spatial representation of the tree positions (red dots) projected onto the 2-D seismic grid (black). The black circle surrounds the trees with three-component velocimeters. Extra Z-land sensors were positioned at the bottom of each of these trees, for deconvolution purposes. The horizontal blue lines correspond to the GPR survey with 23 lines inside the forest and three lines in the open field.

the characteristic aspects of the frequency-dependent propagation regime.

Taking advantage of the METAFORET data, we demonstrate here how a 'trees-in-the-ground' metamaterial configuration degenerate the low frequency (10–100 Hz) surface waves into bulk modes, taking into account the reality of a natural soil and the imperfection of a collection of non-identical trees in a forest. Whereas the Roux *et al.* (2018) study mainly considered the dispersion curve as a signature of the metamaterial behaviour, we look here at spectral intensity ratio, attenuation and scattering length as well as surface wave polarization in regards to the trees resonance. We quantitatively compare the surface wave conversion results obtained through advanced array processing to numerical simulations. The subsurface properties, as in most geophysical system, play an important role in the surface wave dynamics. Our goal is to bring clues on the effects of the trees resonance, untangled from soil properties. This study differs also from previous laboratory-scale investigations involving quasi-perfect man-made metamaterials and quantitatively validate the intuitive metamaterial behaviour of the forest firstly given by Roux *et al.* (2018).

2 EXPERIMENTAL CONFIGURATION OF SEISMIC NETWORKS, VIBRATOR SOURCE AND THE GROUND-PENETRATING RADAR SURVEY

The experiment covers an area of 120 m $\times$ 120 m (Fig. 1a). Measured along one side, there was 90 m of state-managed pine-tree

forest and 30 m of an adjacent agricultural field where small canola plants were being grown at the time of the deployment. The coordinate x is oriented parallel to the 120-m forest edge, and y is perpendicular to this forest edge (Fig. 1a). The trees were grown along regular lines in the x-direction, with a 4-m line interval in the y-direction (Fig. 1b). The intraline tree distances are less regular, with $\Delta x \sim 2.5$ m on average. To facilitate the seismic deployment and the GPR subsurface investigation, the inter-line brush was cleared of vegetation.

The seismic network consists of 961 vertical-component 5-Hz geophones complemented by 100 three-component 4.5-Hz geophones, and 10 three-component short-period velocimeters attached to a set of tree trunks at 2 m above the ground (Fig. 1b). We recorded continuously for 2 weeks, time of the full experiment, which includes active shots recorded during day times. In practice, we performed the ambient noise measurements during night times in order to avoid signal pollution from active shots during day times. The 961 vertical geophones were spatially organized on a grid system made up of 31 lines and 31 columns, with 4-m interelement spacing in both the x-direction and y-direction. The grid sampling was strengthened by data from 100 three-component geophones, as a 100-m line array with constant 1-m spacing (Fig. 1a, purple crosses '+' in the vertical line in the middle of the array). This was located in the central $x = 60$ m and extended from $y = 20$ m to $y = 120$ m, where $y = 90$ m marks the field–forest boundary. In addition to the deployment of this seismic array, six three-component velocimeters were temporally deployed on one single tree (Fig. 1b, black circle), to determine the tree-ground wavefield interactions and modal

vibration of one tree specimen, and then 10 three-component short-period velocimeters were attached to a set of tree trunks at 2 m above the ground, whereby each tree is considered as a resonator under ambient noise vibration and active source excitation.

The vibrator source was a 70-kg continuous vertically-forced mechanical system that excites a 60-s-long, 10- to 100-Hz frequency-modulated sweep. We sequentially activated the vibrator source at 125 different positions (purple crosses 'x' in Fig. 1a) during the 2 weeks of the experiment. The output gain of the continuous system was set adaptively to prevent saturation of the recorded signals from the geophones located next to the vibrator source. The sweep emission was recorded at each sensor of the seismic network, and further cross-correlated with the emitted sweep for the pulse compression. This signal processing methodology (i.e. transmission of a frequency-modulated sweep that is cross-correlated at each receiver with the emitted signal) mimics the transmission of a loud and broadband pulse in the bandwidth of interest.

The GPR data were acquired along 120-m-long lines within the seismological network using shielded 500-MHz antennas. The objective of the GPR survey was to assess the layered subsurface structure, to allow for further interpretation of the seismic signals recorded. A combination of 26 lines were recorded parallel to the forest–field interface (sampling along the *x*-axis, with a 4 m interval along the *y*-axis between two lines), with 23 lines inside the forest and three lines in the canola field (Fig. 1b, blue horizontal lines). The goal was to image the main horizontal interfaces within the top 2 m below the ground.

3 DATA ANALYSIS AND INTERPRETATION

3.1 Subsurface structure and seismic tomography

We process all of the GPR profiles in the same way; namely: (i) [200–700 MHz] band-pass filter; (ii) migration; (iii) time to depth conversion and (iv) late arrivals amplification with time gain (Cassidy & Jol 2009). For processes (ii) and (iii), we use a velocity of 7.6 cm ns^{-1}, as obtained from the average of several semblance velocity analyses performed on several common middle-point acquisitions. The example of a 120-m-long GPR profile in Fig. 2(a) shows a large number of reflectors throughout the entire profile for the first 2 m in depth, the continuity of which is not obvious. The decrease in reflectivity at depths >1.7 m might be related to the presence of the water table. We observe the same subsurface structures both in the forest and the field, with a set of reflectors that do not appear to be continuous along the entire site. A soil pit was locally excavated down to 2.5 m to provide a link between soils attribute measurements and local reflectors detected by GPR data. The soil analysis reveals a highly compacted sand interface located from ∼50 cm to 1.5 m below the surface. Farmers damage this layer for agricultural purposes, and in particular to allow water drainage into the ground. In the absence of reflector continuity, we perform a spatial correlation function on the collection of all of the GPR profiles, which highlights a horizontal decorrelation length of about 2 m (Fig. 2b). This decorrelation length prevents the construction of a pseudo-3-D view of the subsurface layering heterogeneities for the whole site from the combination of parallel GPR profiles.

On the basis of the dense seismic array and the set of active sources, we built two average seismic sections in Fig. 3 for two different frequency bands. Assuming in the first-order approximation spatially uniform elastic properties of the ground with no lateral
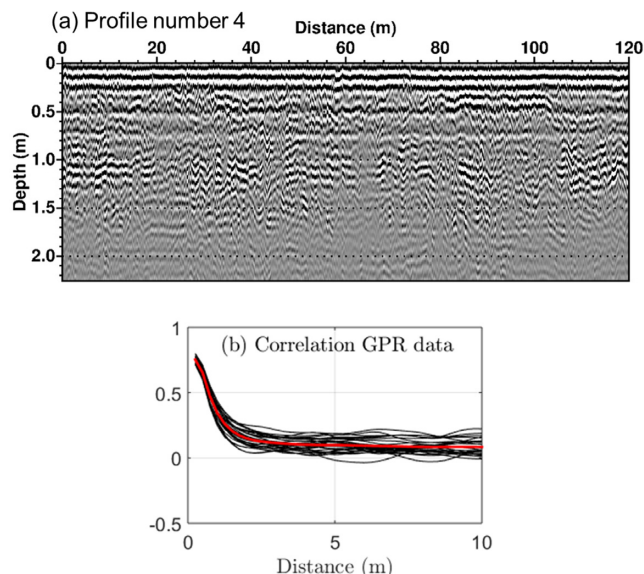

Figure 2. Ground-penetrating radar images obtained before migration at 500 MHz. (a) Line 4 (inside the forest). (b) Average time correlation coefficient with distance (red curve) over the full set of ground-penetrating radar profiles (black curves).

heterogeneities, the frequency-filtered source-to-receiver signals are stacked in 4-m-distance bins, to obtain a spatially averaged representation of the distance-versus-time recorded wavefield.

When filtered below 45 Hz (Fig. 3a), the average seismic section mostly reveals high-amplitude surface waves from which the travel-time propagation can be extracted. This confirms that velocity fluctuations and tree scattering are weak at low frequency. Above 45 Hz (Fig. 3b), a direct/refracted *P* wave is visible, as well as a reflected *P* wave from a deeper interface (depth ∼45 m). The surface wave amplitude is clearly degraded in the stacking process, which confirms that spatial coherence of surface waves is weaker at higher frequency. This might represent the signature of scattering events that are associated with the trees, which behave as strong scatterers at short wavelengths.

We compute the surface wave tomography for the frequency-filtered signals around 30 Hz (Fig. 4). The Rayleigh wave arrival time is extracted from each individual source-to-receiver seismogram. The combination of all sources and all receivers provides efficient ray coverage of the experiment area. The tomography map shows slightly lower velocities in the field than in the forest, which might be interpreted as soil compaction due to the tree roots in the forest. The average surface wave velocity at 30 Hz is 335 m s^{-1}, which corresponds to a ∼11-m wavelength. Thus, the surface wave wavelength is much larger than the size of the heterogeneities highlighted with the GPR (of typical size ∼1 m at depth ∼0.5–1.5 m, see Fig. 2), which make them invisible in the tomography inversion.

3.2 Resonance frequencies of the trees

We carried out two different experiments for the dynamic characterization of the trees. The aim of the first experiment was to record the ambient vibrations in a single tree, which can be considered to be representative of the forest. A set of six broad-band velocimeters were installed along the trunk of this single tree for 8 hr, from the bottom to 6 m in height, with horizontal components perpendicular to the tree axis (Fig. 5a). From this data set, we perform a modal analysis from the singular value decomposition of
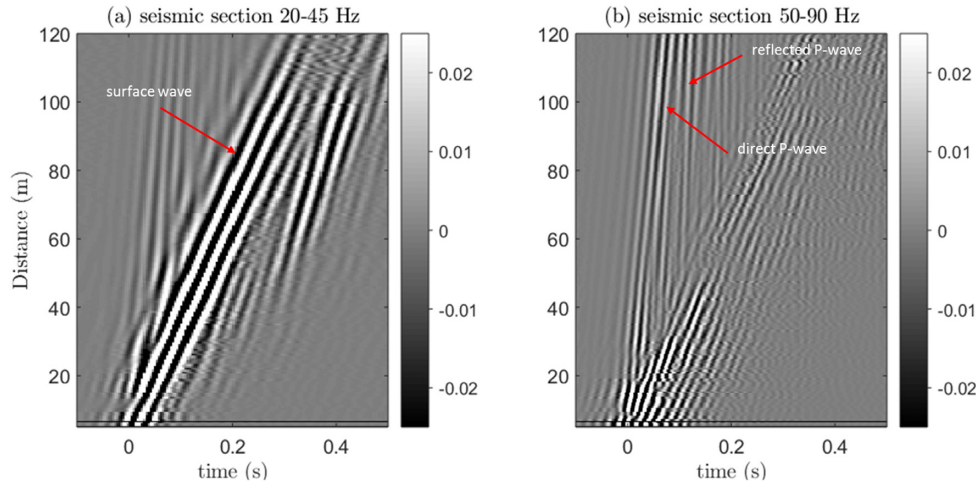
Figure 3. Average seismic section obtained from the full set of 31 × 31 vertical sensors and 125 active sources filtered at 20–45 Hz (a) and 50–90 Hz (b).
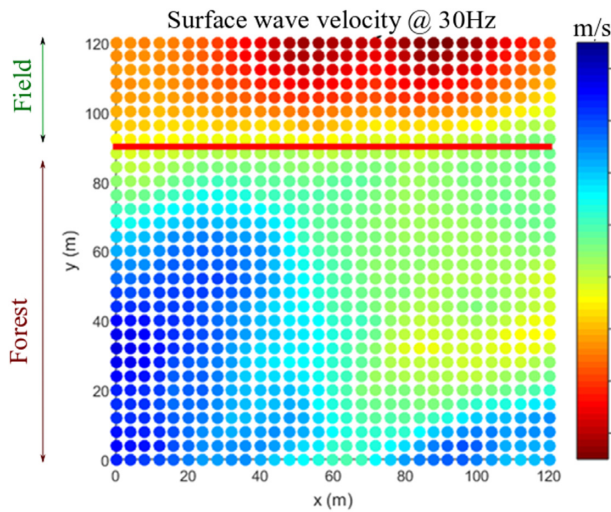

Figure 4. Surface wave tomography using the 31 × 31 vertical sensors at 30 Hz (*Z*-axis). The bold red line represents the limit of the forest, and the colourbar correspond to surface wave velocity in m s^{-1}.

the spectral density matrix calculated from the ambient vibration recordings (Brincker *et al*. 2001). The peaks of the first singular values represent modes where the modal form is the first corresponding singular vector. This method is usually applied to civil-engineering structures (e.g. Michel *et al*. 2010; Guéguen & Bard 2005; Guéguen & Colombi 2016; Chatelainet *et al*. 2000), and it provides the frequencies and depth-dependent modal amplitudes of the system. As well as the low-frequency modes (<10 Hz) identified as fundamental and higher (horizontal) bending modes (Roux *et al*. 2018), a low-Q factor compressional mode was isolated around ∼45 Hz (Fig. 5b). In analogy with the laboratory experiments (Rupin *et al*. 2014; Colquitt *et al*. 2017), this compressional mode opens a frequency band-gap and certainly has a key role in the damping of the surface waves.

The second experiment consisted of monitoring ten different trees, with the instrumentation at a height of 3 m. Figs 5(c) and (d) shows the horizontal and vertical Fourier spectra of the tree vibrations recorded during forced vibration sequences with the vibrator sources. We plot the average power spectral densities of the trees for all of the sources in red. The confidence interval (shaded area in grey) is computed as the standard deviation of the averaging

process over all the actives sources and receivers attached to the set of ten trees. The horizontal component is the average of the two radial and tangential components of the recorded vibrations. Note that the ambient noise also participates in the measurement at frequencies below 10 Hz. We also observe a vertical energetic compression mode around 45 Hz, which is stronger for the vertical component, while all of the trees have about the same frequency behaviour.

3.3 Spectral intensity ratio between the forest and the field

Strong evidence of the role of the trees in the propagation of surface waves can be demonstrated by the spectral ratio between the seismic intensities measured separately in the forest and the field. For each active source, we calculate the power spectral density for the vertical component of the wavefield, and spatially averaged in both areas. The spectral intensity results from the ratio between the forest and the canola field, and this ratio is further averaged over all of the active sources (Fig. 6). Through this calculation, we assume that the range sensitivity to the source variability is smoothened out in the averaging processes performed on both the receivers and the sources. Fig. 6 illustrate the final result with a confidence interval computed as the standard deviation of the averaging process over all the actives sources and receivers (blue area in Fig. 6). The trees response (grey curve in Fig. 6) is added for sake of comparison. It reveals strong damping inside the forest at the resonance frequency of the trees. Such a band-gap is expected in locally resonant metamaterials (Rupin *et al*. 2014; Colombi *et al*. 2016a). The increase in the intensity ratio prior to the tree resonance frequency is also typical of metamaterial behaviour (Colombi *et al*. 2016a). The frequency range of the band-gap extends from 40 to 60 Hz, after which the intensity ratio increases again. Above 60 Hz, surface waves are scattered by local heterogeneities, and the field contribution is dominated by body waves (Fig. 2b), which complicates the interpretation of the spectral intensity ratio.

3.4 Two-point correlation function of the seismic wavefield

To understand further the role of the trees in the amplitude of the wavefield, we calculate the ensemble-averaged two-point correlation function $C(\omega, dr)$ at frequency ω, and for all possible receiving
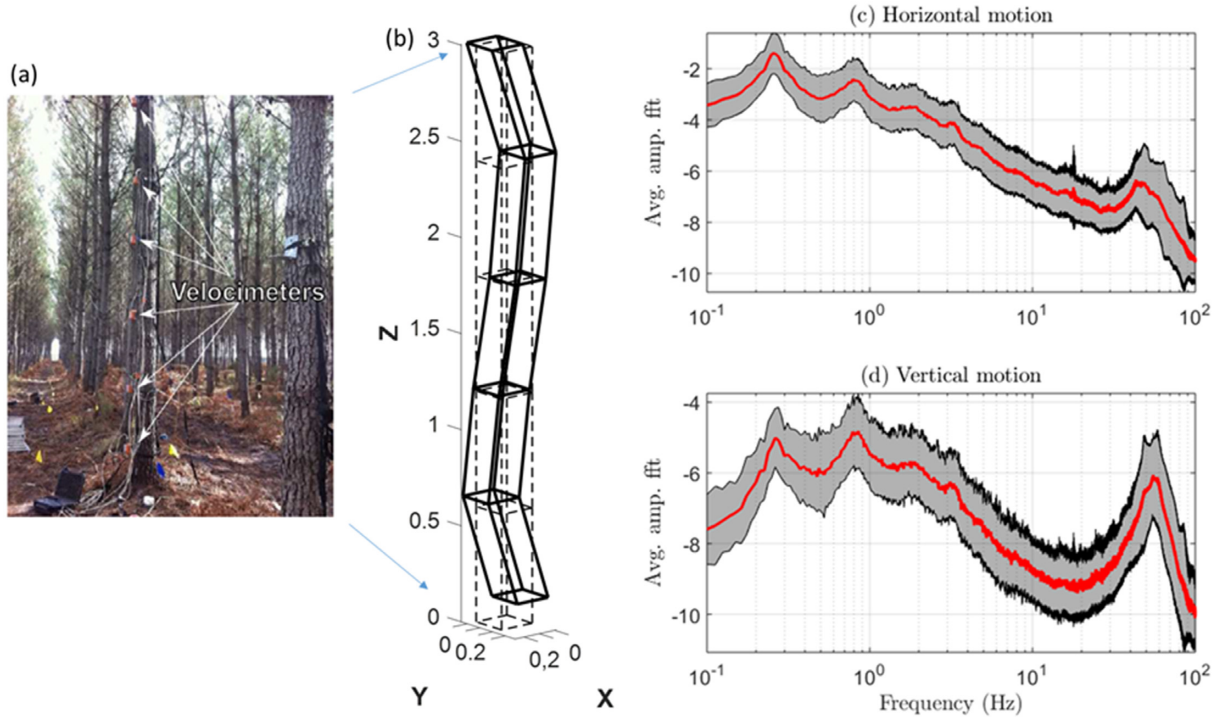
Figure 5. Trees as resonators. (a) Photograph of the tree with velocimeters. (b) Modal shape extracted through singular value decomposition at the compressional resonance (~50 Hz) for a single tree. (c, d) Normalized Fourier spectra averaged for 10 such trees and all sources, for the vertical (c) and horizontal (d) components in red with a confidence interval depicted as a shaded area in grey.
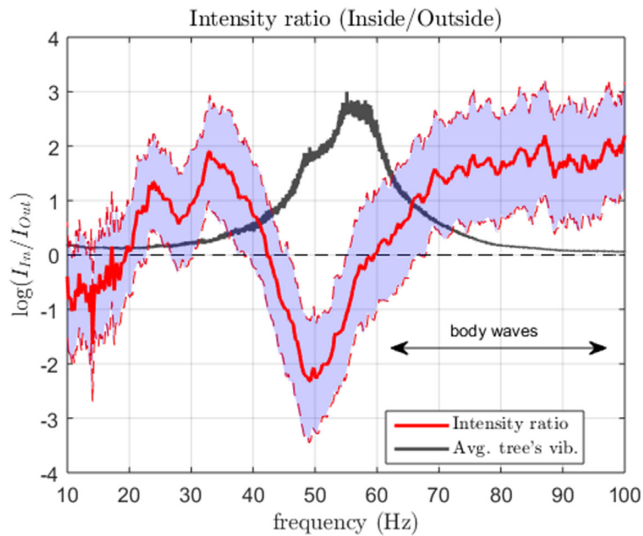

Figure 6. Spectral Intensity ratio (red curve) between the forest (I_{in}) and the canola field (I_{out}) plotted together with the average tree response (grey curve). The blue area corresponds to the standard deviation around the average intensity ratio. The black arrow points out the frequency interval where body wave contribution cannot be omitted.

points separated by distance dr inside the forest. The two-point correlation function is calculated between points $\vec{r}$ and $\vec{r} + d\vec{r}$ inside the forest area:

$$C(\omega, d\vec{r}) = \frac{\langle \Psi(\omega, \vec{r})\Psi^*(\omega, \vec{r} + d\vec{r})\rangle_{\vec{r}}}{\langle |\Psi(\omega, \vec{r})|\rangle_{\vec{r}}}, \tag{1}$$

where $\Psi(\omega\vec{r})$ is the wavefield measured at the angular frequency ω between a source and a geophone separated by distance $\vec{r}$. We

then take advantage of the spatial distribution of the receivers and active sources in the area to average the two-point correlation over all azimuth θ:

$$C(\omega, dr) = \langle C(\omega, d\vec{r})\rangle_{\theta}. \tag{2}$$

Thus, the ensemble-averaged two-point correlation function $C(\omega, dr)$ results from an averaging process that is performed from the set of positions (x,y) of all of the receiving points and active sources located inside the metamaterial, from which the interdistances dr are calculated. The real part of the two-point correlation function $C(\omega, dr)$ is plotted in Fig. 7(a) between 20 and 50 Hz, where the surface waves dominate the wavefield.

We model $C(\omega, dr)$ with the 2-D Green's function that is defined, in the case of a surface wave propagating in a half-space, as:

$$C(\omega, dr) \approx H_0^{(2)}(k_{eff} dr), \tag{3}$$

where $H_0^{(2)}$ is the Hankel function and $k_{eff} = \Re(k_{eff}) - i\Im(k_{eff})$ is the effective wavenumber for the Rayleigh wave. In practice, the effective phase velocity can be deduced from $c_{eff} = \frac{\omega}{\Re(k_{eff})}$. The effective phase velocity c_{eff} is plotted (blue diamonds) in Fig. 7(b) and will be discussed later. The imaginary part of the effective wavenumber $\Im(k_{eff})$ accounts for the scattering attenuation as the intrinsic attenuation (due to viscous loss in the medium) is cancelled out by the normalization factor at the denominator of eq. (1). The scattering attenuation is mainly caused by tree scattering inside the forest. It is classically interpreted as an attenuation length $\ell = 1/\Im(k_{eff})$, that corresponds to the average distance between scatterers in the medium (Lott & Roux 2019).

As shown in Fig. 7(c), good agreement is observed between the modeled Green's function and the experimental two-point correlation function $C(\omega, dr)$. Compared to the spectral intensity ratio shown in Fig. 6, $C(\omega, dr)$ varies with inter-receiver distance dr
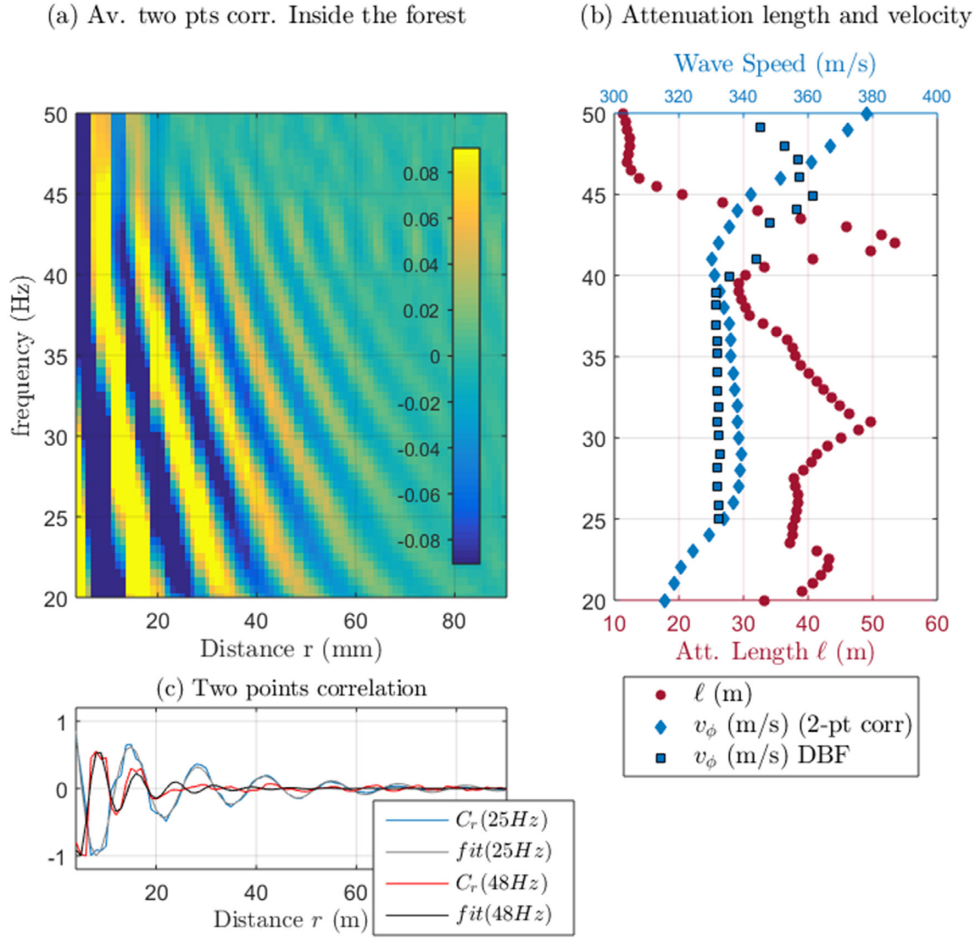
Figure 7. (a) Average two-point correlation as function of frequency measured inside the forest. (b) Attenuation length (red circles) and phase velocity (blue diamonds and blue square for the 2-pts corr. and DBF measurements respectively) inside the forest *versus* frequency. (c) Real part of the correlation function (blue, red) for two frequencies (25, 48 Hz), and the corresponding modeled Green's functions (grey, black).

and accounts for range-dependent wave-diffraction physics. At first sight, we observe a large attenuation length ℓ with $\ell > 2\lambda$ between 20 Hz and 40 Hz that corresponds to a weak attenuation of the coherent wavefield. However, a sudden decrease in the attenuation length down to $\ell \sim \lambda \sim 10$ m coincides with the compressional resonance frequency of the trees at ~45 Hz (red dots in Fig. 7b). The abrupt change in ℓ is in agreement with the strong damping observed on the spectral intensity ratio (Fig. 6). This is another signature of a locally resonant seismic metamaterial in agreement with similar experiments on plates at the laboratory scale (Lott & Roux 2019).

4 DISPERSION CURVE AND POLARIZATION ANALYSIS OF SURFACE WAVE MOTION THROUGH DOUBLE BEAMFORMING

We now study the seismic wavefield behaviour around 45 Hz in more detail, where the compressive resonance frequency of the trees appears to have a major role in the metamaterial interpretation of the tree forest. We focus on the three-component line array (Fig. 1a, black crosses) located at the centre of the area ($x = 60$ m) that extends inside the forest from $y = 20$ to 90 m (1-m spacing between geophones).

Inside the forest, an ensemble of 35 active sources were successively excited along the line array, with 2-m spacing between each source. As shown in Fig. 1, a source subarray made of $N = 5$ neighbouring active sources is considered from a receiver subarray made of $M = 9$ neighbouring receivers. The two subarray apertures are comparable (8 m). The source–receiver subarray pairs are chosen such that the distance between the subarray centres is always >20 m. The use of subarrays aligned along the same direction inside the forest allows the extraction of the Rayleigh wave component from the total wavefield through a double beamforming (DBF) process. DBF was recently applied to dense seismic networks to extract surface wave components from either active sources (De Cacqueray et al. 2011; Boué et al. 2013) or ambient noise correlations (Boue et al. 2014; De Cacqueray et al. 2015; Roux et al. 2016; Wathelet et al. 2018). Following the same procedure, the goal is to time-delay and coherently stack the $N \times M$ source–receiver signals according to: (1) the distance between each source and each receiver and (2) the Rayleigh wave slowness in the propagation medium. The DBF result is an average time-domain signal that solely contains the Rayleigh wave packet between the centres of the two subarrays. A search can be made for the best medium slowness that optimizes the amplitude of the DBF wave packet at different frequency intervals. Through the slowness optimization, the DBF provides an optimal slowness for Rayleigh wave propagation in the forest, from which a dispersion curve can be plotted (Fig. 7b, blue squares).

The dispersion curves obtained from DBF and the two-point correlation function show similar effective wave speed for frequencies up to the trees resonance (∼45–55 Hz) where a sudden change of phase velocity is observed. (Fig. 7d, blue squares and diamonds, respectively). The strong average process over the space and direction of the two-point correlation method provides better resolution of the ground properties compared to DBF, which is only computed along one line in the forest and on a set of a few receivers and sources. On the other hand, the DBF method makes spatial filtering of the waves possible by selecting the slowness range values. Above 45 Hz, the two-point correlation technique becomes sensitive to a higher-order surface wave and bulk modes that are filtered out with DBF (Fig. 7b). Note also that there is no slowdown of the surface wave speed at the low edge of the band-gap, as numerically and theoretically observed in a previous study (Colombi *et al.* 2016a,b, 2017); there is instead an increase. This might be due the interplay of the surface with the bulk modes in the frequency range of the compressional resonance of the trees in this specific case of a heterogeneous layered soil (Fig. 2a).

In the following, we focus on the polarization analysis of the fundamental mode <60 Hz. For this purpose, we need the three components of the geophones along the line array. The DBF algorithm is applied separately on the three-component wavefield recordings to identify and extract the radial and vertical Rayleigh wave components from the wave speed selection. From there, the Rayleigh wave particle motion is reconstructed and finally matched to an ellipse that is characterized by the major and minor axes of *a* and *b*, respectively. The ratio b/a shows a rapid transition around 40 Hz, from $b/a \sim 1.0$ to $b/a \sim 0.4$, which confirms that the Rayleigh wave is converted into a shear-like polarized wave. Above 45 Hz, the fundamental mode is no longer dominant, with a small ellipticity ratio (Fig. 8a) and wave amplitude coherence close to zero (Figs 7a and c). Conversion of the Rayleigh waves into shear bulk waves at the resonance frequency of the trees was theoretically predicted and numerically observed in the context of spatially varied (graded) seismic metamaterial for a homogeneous semi-infinite elastic medium (Colquitt *et al.* 2017; Colombi *et al.* 2017a). The sudden change in the particle motion is further evidence of the tree effects on the surface wave propagation, which confirms the metamaterial behaviour of the forest of trees. Note that the conversion was also demonstrated at the laboratory scale for surface waves propagating in an aluminum sample (Colombi *et al.* 2016b).

5 NUMERICAL SIMULATIONS

Finally, we carry out an inversion of the soil properties procedure and 2-D numerical elastic simulations, which mimic the three-component line set-up, to verify the actual mechanical effects of the trees when untangled from the subsurface soil structure.

First, the subsurface ground structure was determined from surface wave velocity inversion using the Geopsy software (http://www.geopsy.org/). This public code uses the velocity dispersion properties of surface waves; and looks for the best values of the *S*-wave velocity, density, and thickness for a determined set of subsurface layers. Details of the inversion procedure can be found in Wathelet *et al.* (2004) and Wathelet (2008). The inversion process needs the *a priori* number of layers, and ends up with the 'best-fitting' results, which updates the thickness layers and their mechanical properties (Figs 9a and b). The experimental dispersion curve is plotted in Fig. 9(a) (black dots). For each of the three-layer shear velocity profile (Fig. 9b, brown to green curves), a theoretical

dispersion curve is computed (brown to green curves in Fig. 9a) and compared to the experimental one. Inside the forest, the inversion is constrained by the concavity of the dispersion curve around 30 Hz (Fig. 9a) that supports the presence of a compacted sand layer (higher shear wave speed between 2 and 4 m on the green curve in Fig. 9b) close to the subsurface that was also revealed by GPR measurements. The lack of depth resolution close to the surface is due to the finite frequency band (20–40 Hz) used for the surface wave inversion process. From these results, it can then be asked what are the respective roles of the trees and the subsurface-layered medium on the surface wave polarization analysis shown in Fig. 8.

To understand this potential trade-off, the SPECFEM2D software (Komatitsch & Tromp 1999; Guéguen & Martin 2007) can be used to tackle complex model geometries with subwavelength resonators and layered-soil properties. The code is heavily parallelized, and it computes elastic wavefields with a high level of spatial and temporal detail. SPECFEM2D solves the plain strain elastic problem (i.e. P-SV polarization) for a half-space elastic domain with a free surface at the top edge and perfectly matched conditions on the remaining lateral and bottom boundaries. The source is implemented as in the experiment with a vertical force, using a Ricker source–time function centred at 50 Hz. The trees are modeled as longitudinally elongated beams (i.e. cantilever beams) attached without discontinuities to the surface of the half-space. The soil and trees are characterized by very different mechanical properties (e.g. Young modulus, Poisson ratio and density). The correct choice of these parameters is of crucial importance to understand the actual seismic observations (Colombi *et al.* 2016a).

When excited by a broad-band pulse centred at 50 Hz the resonators are characterized by both flexural and compressional resonances, with a dynamic response that mimics those of the actual trees in the forest (not shown here). The depth-dependent velocity model obtained from the surface wave inversion (Fig. 9b) is then implemented into the SPECFEM simulation software as ground properties (Fig. 10). We perform two simulations of a propagating pulse at the surface of the computational domain: one with and one without the tree-like resonators. We process the numerical data with the same procedure as the experimental ones: the DBF method is applied for one set of seven sources and seven receivers, with a 50-m subarray distance.

We confirm the strong change in the surface wave polarization through these SPECFEM simulations. The no-tree simulation shows that for a multilayered soil, changes in ellipticity do occur, but at higher frequencies (>55 Hz, Fig. 8a), while in the simulation with trees, the effects are clearly located in the 40–50 Hz tree's resonance frequency band, with a drop in the *b/a* ellipticity ratio from 1.0 to <0.5 (Figs 8b and c). After 60 Hz, the tracked surface wave no longer exist because of a conversion into bulk modes.

6 DISCUSSION

The cross comparison of the multiphysic data set is the key to understand the surface wave dynamics occurring in the METAFORET experiment. First, we need to remind the expected surface wave behaviour in the ideal case of a homogeneous half-space, coupled to a collection of tree-like resonator. Around the compressional resonance of the resonators, numerical simulations show that surface wave slows down up to a point where no movement is allowed on the substrate surface, and then surface wave converts into bulk shear wave (Colombi et al. 2016a, 2017b).
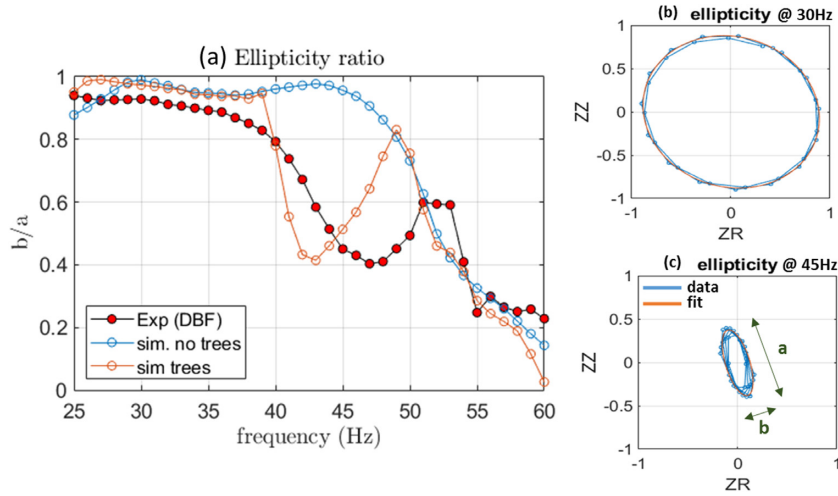
Figure 8. Double beamforming results. (a) Ellipticity ratio of the reconstructed particle motion through the double beamforming technique. (b, c) Example of reconstructed particle motions at 30 Hz (b) and 45 Hz (c) from experimental data.
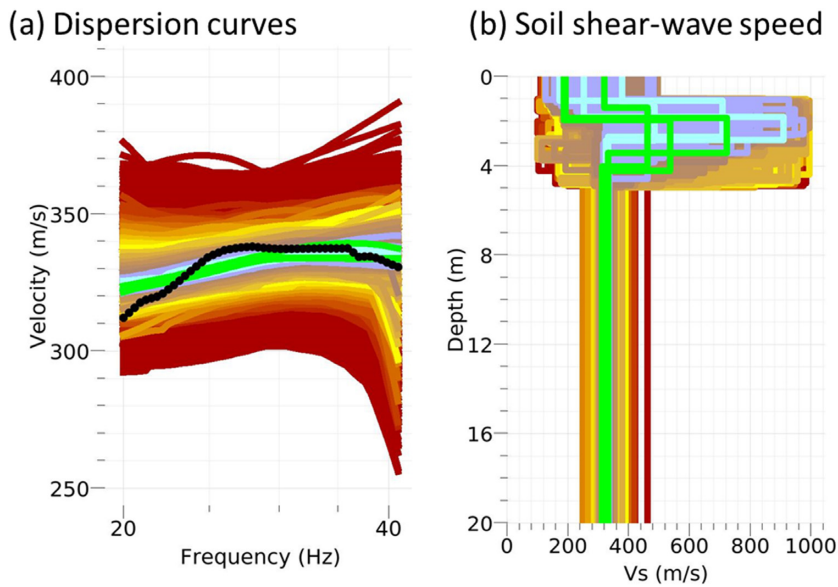

Figure 9. Numerical simulation results using the Geopsy software. (a, b) Starting with an experimental measurement of the surface wave speed versus frequency (black dots), the inverted dispersions curves are computed iteratively (a) (brown to green, high to low misfit) from a ground shear wave speed model (b).
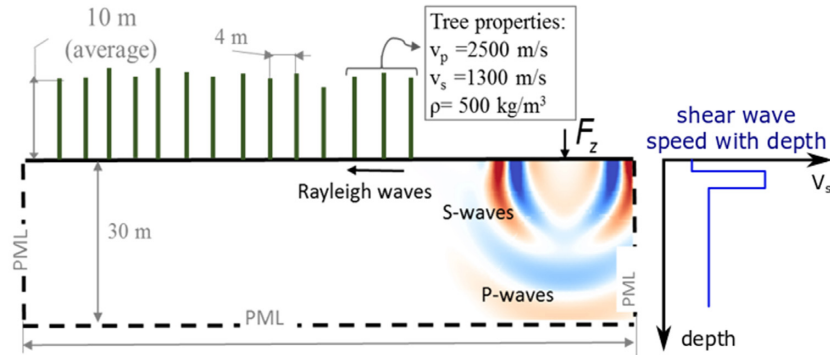

Figure 10. 2-D dynamic simulation with a mimicked forest. The average ground property is implemented in the SPECFM2D within two simulation boxes: with and without the trees.

In the present seismic scale experiment, the behaviour differs somehow. Both the GPR survey and the surface wave dispersion curve highlights some layering property of the soil substrate inside the forest. For this reason, several surface modes can exist and the trees may then produce a leakage through those higher order modes. The difficulty is so to untangle the sublayering soil effect from the trees one.

Two main results of the METAFORET experiment agree with the above-mentioned literature, given the limitations of this seismic experiment to reproduce the full Rayleigh-to-shear wave leakage that is observed at the laboratory scale (Colombi *et al.* 2016b). First, the attenuation length, described in Section 2.4, reveals a strong damping at the compressional resonance. Secondly, the surface wave polarization varies over more than 50 per cent at the same frequency, confirming the leakage to higher order modes. The simulations with and without the trees finally confirm the feedback induced by the resonators on the soil along the surface wave propagation.

7 CONCLUSION

In this paper, we focus on the behaviour of surface wave modes that can arise in a layered subsurface structure coupled to subwavelength resonators. It brings a step forward the analysis of Roux *et al.* (2018) with multiphysics cross-measurements and numerical simulations that can help to untangle the effects of the soil substructure from the trees resonance. In particular, the coupling between fundamental and higher-order surface modes is evidenced around the trees resonance frequency, taking into account attenuation length, spectral energy ratio and surface wave polarization. Two mains results should be underlined. First, we observe strong attenuation in the two-point correlation functions at the compressional resonance frequency of the trees. This attenuation arises from the incoherent scattering associated with the surface wave–trees interaction, as revealed also by the energy spectral ratio between the forest and the free field. Secondly, another obvious sign of the resonance effect of the trees on the surface wave propagation is the change in the particle motion ellipticity at frequencies close to the resonance of the trees. Despite the surface waves being clearly affected by the tree resonances, there is no evidence of a band-gap in the sense of a sudden and strong damping and total wave reflection at the forest interface. Here, by looking at the three components of the wavefield, we can conclude that the trees create a leakage that affects a higher-order surface mode that is characterized by a different type of polarization. Finally, the reality of the heterogeneous geophysical substrate below the forest ultimately underpins the behaviour of this locally resonant metamaterial.

ACKNOWLEDGEMENTS

REFERENCES

Achaoui, Y., Khelif, A., Benchabane, S., Robert, L. & Laude, V., 2011. Experimental observation of locally-resonant and Bragg band gaps for surface guided waves in a phononic crystal of pillars, *Phys. Rev. B,* **83**(10), 104201.

Boué, P., Roux, P., Campillo, M. & de Cacqueray, B., 2013. Double beamforming processing in a seismic prospecting context, *Geophysics,* **78**(3), V101–V108.

Boué, P., Roux, P., Campillo, M. & Briand, X. 2014. Phase velocity tomography of surface waves using ambient noise cross-correlation and array processing, *J. geophys. Res.,* **119**, 519–529.

Brincker, R., Zhang, L. & Andersen, P., 2001. Modal identification of output-only systems using frequency domain decomposition, *Smart Mater. Struct.,* **10**(3), 441.

Brûlé, S., Javelaud, E.H., Enoch, S. & Guenneau, S., 2014. Experiments on seismic metamaterials: molding surface waves, *Phys. Rev. Lett.,* **112**(13), 133901.

Brun, M., Guenneau, S. & Movchan, A.B., 2009. Achieving control of in-plane elastic waves, *Appl. Phys. Lett.,* **94**(6), 061903.

Cassidy, N.J. & Jol, H.M., 2009. Ground penetrating radar data processing, modelling and analysis, in *Ground Penetrating Radar: Theory and Applications,* ed. Jol, H.M., pp. 141–176, Elsevier Science.

Chatelain, J.L., Gueguen, P., Guillier, B., Frechet, J., Bondoux, F., Sarrault, J. & Neuville, J.M., 2000. CityShark: a user-friendly instrument dedicated to ambient noise (microtremor) recording for site and building response studies, *Seismol. Res. Lett.,* **71**(6), 698–703.

Colombi, A., Roux, P., Guenneau, S., Gueguen, P. & Craster, R.V., 2016a. Forests as a natural seismic metamaterial: Rayleigh wave bandgaps induced by local resonances, *Sci. Rep.,* **6**, 19238.

Colombi, A., Colquitt, D., Roux, P., Guenneau, S. & Craster, R.V., 2016b. A seismic metamaterial: the resonant metawedge, *Sci. Rep.,* **6**, 27717.

Colombi, A. *et al.*, 2017a. Enhanced sensing and conversion of ultrasonic Rayleigh waves by elastic metasurfaces, *Sci. Rep.,* **7**(1), 6750.

Colombi, A., Craster, R.V., Colquitt, D., Achaoui, Y., Guenneau, S., Roux, P. & Rupin, M., 2017b. Elastic wave control beyond band-gaps: shaping the flow of waves in plates and half-spaces with subwavelength resonant rods, *Front. Mech. Eng.,* **3**, 10.

Colquitt, D.J., Colombi, A., Craster, R.V., Roux, P. & Guenneau, S.R.L., 2017. Seismic metasurfaces: sub-wavelength resonators and Rayleigh wave interaction, *J. Mech. Phys. Solids,* **99**, 379–393.

De Caqueray, B., Roux, P., Campillo, M., Catheline, S. & Boue, P., 2011. Elastic-wave identification and extraction through array processing: an experimental investigation at the laboratory scale, *J. appl. Geophys.,* **74**, 81–88.

De Cacqueray, B., Roux, P. & Campillo, M., 2015. Using slowness and azimuth fluctuations as new observables for four-dimensional reservoir seismic monitoring, *Geophys. Prospect.,* **64**(6), 1537–1555.

Engheta, N. & Ziolkowski, R.W.eds, 2006. *Metamaterials: Physics and Engineering Explorations,* John Wiley & Sons.

Farhat, M., Guenneau, S. & Enoch, S., 2009. Ultrabroadband elastic cloaking in thin plates, *Phys. Rev. Lett.,* **103**(2), 024301.

Guéguen, P. & Bard, P.Y., 2005. Soil-structure and soil-structure-soil interaction: experimental evidence at the Volvi test site, *J. Earthq. Eng.,* **9**(5), 657–693.

Guéguen, P. & Colombi, A., 2016. Experimental and numerical evidence of the clustering effect of structures on their response during an earthquake: a case study of three identical towers in the city of Grenoble, France, *Bull. seism. Soc. Am.,* **106**(6), 2855–2864.

Komatitsch, D. & Tromp, J., 1999. Introduction to the spectral element method for three-dimensional seismic wave propagation, *Geophys. J. Int.,* **139**(3), 806–822.

Komatitsch, D. & Martin, R., 2007. An unsplit convolutional perfectly matched layer improved at grazing incidence for the seismic wave equation, *Geophysics,* **72**(5), SM155–SM167.

Krödel, S., Thomé, N. & Daraio, C., 2015. Wide band-gap seismic metastructures, *Extreme Mech. Lett.,* **4**, 111–117.

Liu, Z., Zhang, X., Mao, Y., Zhu, Y.Y., Yang, Z., Chan, C.T. & Sheng, P., 2000. Locally resonant sonic materials, *Science,* **289**(5485), 1734–1736.

Lott, M. & Roux, P., 2019. Effective impedance of a locally resonant metasurface, *Phys. Rev. Mater.,* **3**, 065202.

Michel, C., Guéguen, P., El Arem, S., Mazars, J. & Kotronis, P., 2010. Full-scale dynamic response of an RC building under weak seismic motions using earthquake recordings, ambient vibrations and modelling, *Earthq. Eng. Struct. Dyn.,* **39**(4), 419–441.

Milton, G.W., Briane, M. & Willis, J.R., 2006. On cloaking for elasticity and physical equations with a transformation invariant form, *New J. Phys.,* **8**(10), 248.

Pendry, J.B., 2000. Negative refraction makes a perfect lens, *Phys. Rev. Lett.,* **85**(18), 3966.

Pendry, J.B., Schurig, D. & Smith, D.R., 2006. Controlling electromagnetic fields, *Science,* **312,** 1780.

Rupin, M., Lemoult, F., Lerosey, G. & Roux, P., 2014. Experimental demonstration of ordered and disordered multiresonant metamaterials for lamb waves, *Phys. Rev. Lett.,* **112**(23), 234301.

Roux, P., Moreau, L., Lecointre, A., Hillers, G., Campillo, M., Ben-Zion, Y., Zigone, D. & Vernon, F., 2016. A methodological approach toward high-resolution surface wave imaging of the San Jacinto Fault Zone using ambient-noise recordings at a spatially dense array, *Geophys. J. Int.,* **206,** 980–992.

Roux, P., Bindi, D., Boxberger, T., Colombi, A., Cotton, F., Douste-Bacque, I. & Lecocq, T., 2018. Toward seismic metamaterials: the METAFORET project, *Seismol. Res. Lett.,* **89**(2A), 582–593.

Wathelet, M., 2008. An improved neighborhood algorithm: parameter conditions and dynamic scaling, *Geophys. Res. Lett.,* **35**(9).

Wathelet, M., Jongmans, D. & Ohrnberger, M., 2004. Surface-wave inversion using a direct search algorithm and its application to ambient vibration measurements, *Near Surf. Geophys.,* **2**(4), 211–221.

Wathelet, M., Guillier, B., Roux, P., Cornou, C. & Ohrnberger, M., 2018. Rayleigh wave three-component beamforming: signed ellipticity assessment from high-resolution frequency-wavenumber processing of ambient vibration arrays, *Geophys. J. Int.,* **215**(1), 507–523.